Journal of
Micro/Nanolithography,
MEMS, and MOEMS

Nanolithography.SPIEDigitalLibrary.org

Modeling and measurement of hydrogen radical densities of *in situ* plasma-based Sn cleaning source

Daniel T. Elg
Gianluca A. Panici
Jason A. Peck
Shailendra N. Srivastava
David N. Ruzic

SPIE.

Daniel T. Elg, Gianluca A. Panici, Jason A. Peck, Shailendra N. Srivastava, David N. Ruzic, "Modeling and measurement of hydrogen radical densities of *in situ* plasma-based Sn cleaning source," *J. Micro/Nanolith. MEMS MOEMS* **16**(2), 023501 (2017), doi: 10.1117/1.JMM.16.2.023501.

Downloaded From: https://www.spiedigitallibrary.org/journals/Journal-of-Micro/Nanolithography,-MEMS,-and-MOEMS on 6/13/2018 Terms of Use: https://www.spiedigitallibrary.org/terms-of-use

Modeling and measurement of hydrogen radical densities of *in situ* plasma-based Sn cleaning source

Daniel T. Elg,[a,†] Gianluca A. Panici,[a] Jason A. Peck,[a] Shailendra N. Srivastava,[b,‡] and David N. Ruzic[a,*]
[a]University of Illinois at Urbana-Champaign, Center for Plasma-Material Interactions, Department of Nuclear, Plasma, and Radiological Engineering, Urbana, Illinois, United States
[b]University of Illinois at Urbana-Champaign, Applied Research Institute, Champaign, Illinois, United States

Abstract. Extreme ultraviolet (EUV) lithography sources expel Sn debris. This debris deposits on the collector optic used to focus the EUV light, lowering its reflectivity and EUV throughput to the wafer. Consequently, the collector must be cleaned, causing source downtime. To solve this, a hydrogen plasma source was developed to clean the collector *in situ* by using the collector as an antenna to create a hydrogen plasma and create H radicals, which etch Sn as SnH_4. This technique has been shown to remove Sn from a 300-mm-diameter stainless steel dummy collector. The H radical density is of key importance in Sn etching. The effects of power, pressure, and flow on radical density are explored. A catalytic probe has been used to measure radical density, and a zero-dimensional model is used to provide the fundamental science behind radical creation and predict radical densities. Model predictions and experimental measurements are in good agreement. The trends observed in radical density, contrasted with measured Sn removal rates, show that radical density is not the limiting factor in this etching system; other factors, such as SnH_4 redeposition and energetic ion bombardment, must be more fully understood in order to predict removal rates. *© 2017 Society of Photo-Optical Instrumentation Engineers (SPIE)* [DOI: 10.1117/1.JMM.16.2.023501]

Keywords: extreme ultraviolet; collector; cleaning; *in situ*; plasma; hydrogen; debris.

Paper 16164P received Dec. 2, 2016; accepted for publication Mar. 9, 2017; published online Apr. 7, 2017.

1 Introduction

For decades, the semiconductor industry has doubled the number of transistors per area on integrated circuits every two years. This phenomenon is known as Moore's law.[1] As part of the facilitation of Moore's law, the semiconductor industry typically shrank the wavelength of light used to pattern photoresist in lithography. However, since 2001, this wavelength has stagnated at 193 nm,[2] while the minimum feature size in high-volume manufacturing (HVM) is, at present, 14 nm.[3] The ability to create features far below the lithographic wavelength has been made possible through techniques such as immersion lithography and multiple patterning. However, with every feature shrink, multiple patterning becomes more time-consuming and expensive. Thus, it is desirable to finally shrink the wavelength of light used in lithography.

The most promising candidate for next-generation lithography is 13.5-nm extreme ultraviolet (EUV) lithography, which has been the subject of much research. EUV sources have been demonstrated to successfully pattern wafers; however, they cannot yet do so quickly enough and reliably enough to be economically viable for HVM. Two key parameters that must be increased are the source power and tool availability. While a great deal of progress has recently been reported with regards to these and other parameters, EUV lithography is still not yet at target levels for HVM insertion. Additionally, even once industrial adoption of EUV has taken place, source power will need to be continually increased as the minimum feature size is reduced even further.[4]

In contrast to conventional lithography, which focuses laser light with transparent lenses, EUV lithography produces light with a dense, energetic Sn plasma ($T_e \sim 20$ eV, $n_e \sim 10^{19}$ cm^{-3}) and focuses it with synthetic Bragg reflectors known as multilayer mirrors (MLMs).[5–7] The mirrors consist of alternating bilayers of Mo/Si, each ~6.9-nm-thick, covered with a protective "capping" layer a few nanometers in thickness.[8,9] The first MLM, known as the collector optic, is exposed directly to the EUV-producing plasma; it must collect the EUV light and send it to the rest of the optical chain. One of the many factors negatively impacting both EUV power and source availability is collector contamination with Sn.[10] Since the collector is exposed to the Sn plasma, source operation causes Sn to deposit on the collector, reducing its EUV reflectivity. This, in turn, results in lower EUV power at the wafer, necessitating longer exposure times to provide the necessary exposure dose. Eventually, the collector must be either cleaned or replaced, causing source downtime.

An ideal technique for cleaning the collector would do so *in situ*, obviating the need for venting. Optimally, this technique would also create etching species at the collector surface without any sort of delivery system, maximizing the use of the etchants and allowing for the potential of continued EUV source operation even during collector cleaning. Such a cleaning technique has been developed at the Center

*Address all correspondence to: David N. Ruzic, E-mail: druzic@illinois.edu

†Current Affiliation: University of California, Berkeley, Department of Chemical and Biomolecular Engineering, Berkeley, California, United States

‡Current Affiliation: Applied Materials, Inc., Santa Clara, California, United States

1932-5150/2017/$25.00 © 2017 SPIE

Downloaded From: https://www.spiedigitallibrary.org/journals/Journal-of-Micro/Nanolithography,-MEMS,-and-MOEMS on 6/13/2018 Terms of Use: https://www.spiedigitallibrary.org/terms-of-use

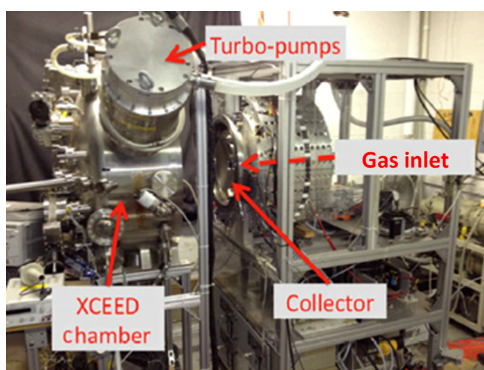

Fig. 1 XCEED is shown with the collector installed. For etching experiments, the chamber (on the cart at left) was attached to the former EUV source (at right). The collector was driven with 300-W 13.56-MHz RF power through an electrical feedthrough, which allowed for electrical connection to the electrically isolated dummy collector.

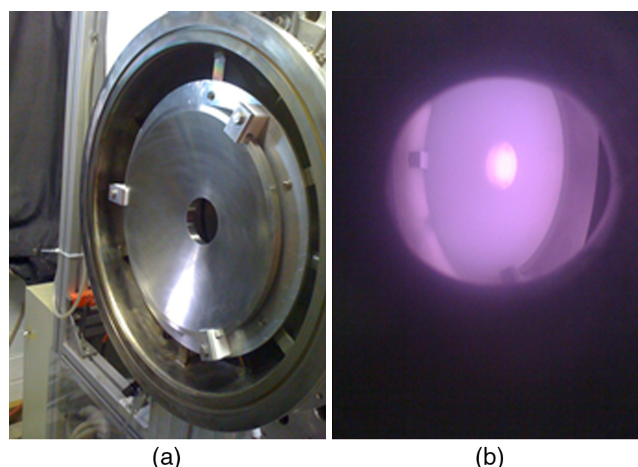

Fig. 2 (a) The collector is installed with electrically isolating Teflon clamps. (b) The collector driving a hydrogen plasma, with the collector itself acting as the antenna.

for Plasma–Material Interactions (CPMI) of the University of Illinois. This technique, detailed in a separate paper,[11] uses the collector itself as a hydrogen plasma source. By attaching an RF supply to the collector, a capacitively coupled hydrogen plasma can be created, creating radicals near the collector surface. These radicals etch Sn by forming gaseous SnH_4 according to

$$Sn(s) + 4H(g) \rightarrow SnH_4(g). \tag{1}$$

This technique has been demonstrated at CPMI. A 300-mm-diameter stainless steel dummy collector has been fully cleaned with removal rates of ~ 1 nm/ min, and EUV reflectivity has been restored to Sn-coated MLM samples on the dummy collector surface.[11]

Previously published work has focused on successful experimental demonstration of the cleaning technique at 65 mTorr and 500 sccm of H_2.[11] However, adoption in a real EUV source will require scaling up to higher pressures and flowrates. In order to understand how best to maximize the removal rate, the fundamental processes underlying Sn removal must be understood. One of those processes is hydrogen radical creation. This paper will focus on the science of radical creation in this plasma source. A zero-dimensional (0-D) plasma chemistry model has been developed to predict radical densities. This model will be shown to be in good agreement with results from a catalytic radical probe, validating the data measured by the probe. Trends in radical densities will be explored as a function of power, pressure, and flow. When compared to measured Sn removal rates, these trends will make clear that radical creation is not the limiting factor governing Sn removal in this plasma source. The results of this paper will show that, in order to maximize Sn removal, the effects of other factors such as SnH_4 redeposition and energetic ion bombardment will need to be understood.

2 Experimental Setup

Plasma experiments were performed in the xtreme commercial EUV exposure diagnostic (XCEED) chamber. XCEED is attached to an XTS 13-35 Xe-fueled z-pinch EUV source and was originally used to diagnose the source output.[12,13] However, for this paper, XCEED was repurposed to hold a 300-mm-diameter stainless steel dummy collector, which was used to drive a capacitively coupled H_2 plasma. The collector was isolated from chamber ground and was supplied with 300-W of 13.56-MHz power. XCEED, the collector, and a circuit diagram are shown in Figs. 1–3. Further information about the source setup is provided in Ref. 11.

Two *in situ* plasma diagnostics were used in obtaining the data presented in this paper. A single RF-compensated Langmuir probe is used to measure electron density (n_e) and electron temperature (T_e). These measurements were used as inputs to the plasma chemistry model. Theory and operation of the Langmuir probe are described in Ref. 14. A catalytic probe was used to measure the radical density. The catalytic probe consists of a thermocouple welded onto a small piece of Au, which has a recombination coefficient of 0.18 for H radicals.[15] Recombination reactions on the surface yield heat; eventually, a steady state is reached where heating equals cooling. At this point, the plasma is turned off, and the recombination heat is removed. The cooling rate at this point is assumed to equal the radical heating rate, and power delivered by radicals is equated to the power due to the temperature change in time

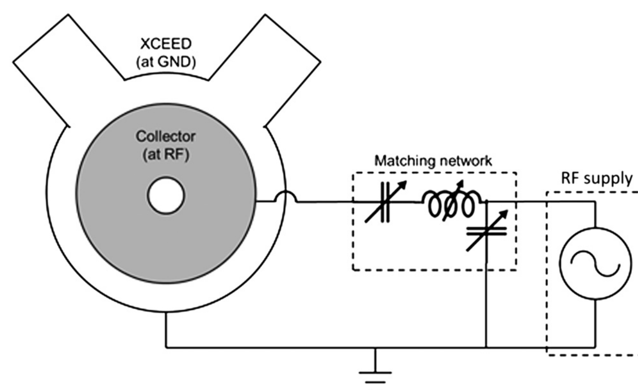

Fig. 3 A circuit diagram of the plasma source setup is shown. The collector is isolated inside XCEED and is attached to a 300-W 13.56-MHz RF supply. A matching network serves to minimize reflected power.

Downloaded From: https://www.spiedigitallibrary.org/journals/Journal-of-Micro/Nanolithography,-MEMS,-and-MOEMS on 6/13/2018 Terms of Use: https://www.spiedigitallibrary.org/terms-of-use

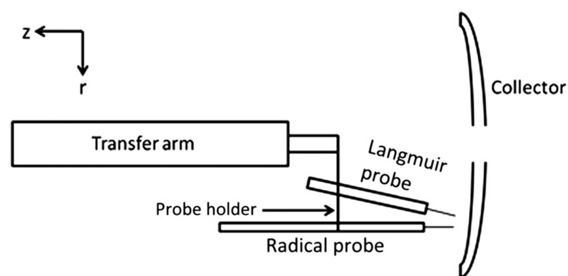

Fig. 4 The Langmuir probe and catalytic radical probe are placed very close together, effectively measuring conditions at the same point. Both are suspended from a transfer arm, which can translate the probes in the axial (z) direction.

$$P = \frac{1}{2} W\gamma \frac{n_H v_{\mathrm{th}}}{4} A_{\mathrm{probe}} = mc_p \frac{\mathrm{d}T}{\mathrm{d}t}, \quad (2)$$

where W is the energy yield per recombination, γ is the recombination coefficient, v_{th} is the thermal velocity of H radicals, A_{probe} is the probe area, m is the mass of the probe, c_p is the specific heat of the probe material, and $\mathrm{d}T/\mathrm{d}t$ is the rate of change in probe temperature immediately after plasma shutoff. The only unknown is the radical density n_{H} which can then be calculated. It should be noted that this method does not take heating by hot ions and neutrals into account. More details about the probe can be found in Refs. 16–18.

Both probes were positioned in front of the collector approximately halfway between the inner and outer radii and were attached to a transfer arm which allowed translation in the axial direction (z-direction), as diagrammed in Fig. 4.

For Sn removal experiments, the dummy collector, along with Si witness plates, was coated with Sn in a magnetron deposition system. Exposure to the H_2 plasma in XCEED was then carried out for 2 h, and the remaining thickness of Sn was measured by a profilometer, yielding Sn removal rates. These experiments were carried out similarly to those detailed in Ref. 11; the only difference was the variation of pressure and flow.

3 Zero-Dimensional Plasma Chemistry Model

3.1 *Model Setup*

To validate the radical probe and understand the science behind radical creation, a simple model was developed. Plasma chemistry modeling is often used to predict densities of species in plasmas. However, a full two-dimensional plasma chemistry model involves (at the least) solving coupled mass continuity equations for every species; momentum balance equations and an electron energy equation are often involved, as well. This kind of modeling is computationally intensive; performing it in a system such as XCEED, in which the pumps do not lie in the same plane as the source, would require even more-intensive 3-D modeling. Such an approach is beyond the scope of a simple model.

A common alternative to provide density predictions with less computational burden is to use a "0-D" model, in which rate equations are solved for plasma species within a given domain. Volumetric reactions provide gains and losses in species density, as do surface boundary conditions, as shown in

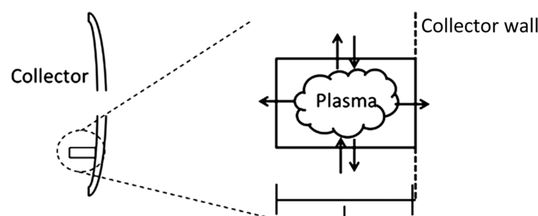

Fig. 5 The domain for the model is shown. Inside the domain, the plasma is assumed uniform. The collector is approximated as a flat surface, and the electron density and electron temperature were measured with the Langmuir probe. The plasma was observed to vary much more sharply in the axial direction than the radial direction, and it was assumed to be uniform in regards to rotation about the center of the collector. Thus, as it was assumed that no net flux occurred across faces of the domain except those in the axial direction (as shown by the arrows in the zoomed-in picture). The method of determining the domain length L, as well as the axial fluxes, is described.

$$\frac{\mathrm{d}n}{\mathrm{d}t} = (\text{gain from reactions}) - (\text{loss from reactions}) - \sum_{\text{boundary}} \frac{A_{\text{boundary}}}{V} \Gamma_{\text{boundary}}, \quad (3)$$

where n is the density of the particular species, V is the domain volume, A is the boundary area, and Γ_{boundary} is the flux of particles out of the domain across a particular boundary (in the case of an influx, this term is negative).

However, 0-D models require various assumptions. Often, densities are taken to be uniform in the entire chamber.[19] In yet another type of 0-D model, some densities are assigned certain nonuniform profiles (e.g., the ion densities are assigned parabolic profiles), but the electron density is still left uniform.[20] Additionally, in this latter method, only volume-averaged densities are calculated. Meanwhile, in order to calculate the boundary fluxes, simple chamber geometries must generally be used.[20–22]

XCEED does not easily fit these approaches. The plasma is very localized at the collector surface, and the chamber is very large; no charged species density, including the electron density, can be approximated as uniform throughout the chamber. Additionally, the geometry does not easily conform to common simple designs. Neither the diameter nor the length of XCEED is significantly larger than the other, the collector (and, thus, the plasma created on its surface) does not extend all the way to the walls of the chamber, and there is a hole in the center of the collector. Thus, constructing a 0-D model that would actively predict radical densities at the surface would prove difficult if the model was applied to the entire chamber. However, uniformity can be approximated for small dimensions, and requirements for a 0-D model should be met if the model is constrained to a small domain.

Thus, a small box in front of the collector was chosen as the domain. In this box, the plasma is assumed uniform. The collector is approximated as a flat surface. The electron density and temperature within the box were determined by Langmuir probe measurements. A diagram of the domain is shown in Fig. 5. Arrows indicate net fluxes to/from the plasma across surfaces; equal opposing arrows indicate no net flux. This will be explained below.

It was necessary to consider boundary conditions and the uniformity approximation when choosing the size of

Downloaded From: https://www.spiedigitallibrary.org/journals/Journal-of-Micro/Nanolithography,-MEMS,-and-MOEMS on 6/13/2018 Terms of Use: https://www.spiedigitallibrary.org/terms-of-use

the domain. Much stronger variation was observed in the z-direction than the r-direction, and the plasma was assumed to be uniform with regards to rotation about the center of the collector. Thus, it was assumed that approximately no net diffusion occurred across the walls of the domain in the nonaxial directions. The only surface losses (or gains) were assumed to occur at the collector surface and through the opposing surface. Since the net fluxes across the other surfaces were thus set to 0, this approximation also simplified the choice of domain size by allowing the nonaxial dimensions to be arbitrary. The size of the domain only enters the model through area-to-volume ratios in the $\frac{A_{\text{boundary}}}{V}\Gamma_{\text{boundary}}$ terms of Eq. (3). Since the only nonzero terms will be from the collector surface and the opposing face, the area-to-volume ratio in all nonzero terms will simply be $1/L$, where L is the axial length of the domain.

L was determined by considering a measured axial electron density profile with 1-cm increments. In order to decouple the domain from other cells, it was necessary to determine an effective "cutoff length" such that the plasma density at smaller lengths could be approximated as uniform and the electron density at larger lengths could be approximated as 0. To take a real, nondigital profile and approximate it with an "on" region and an "off" region, the length was chosen to be the point at which the slope of the density was steepest, signaling a sharp change from high density to low density. According to this procedure, L was set to 9 cm for the 65-mTorr simulations, 6 cm for the 97.5-mTorr simulations, and 5 cm for the 130-mTorr simulations.

3.2 *Volumetric Reactions*

With the assumptions set, a 0-D model was implemented by solving reaction rate equations inside the domain to predict densities of hydrogen radicals and ions. Each reaction occurs with a different rate constant k, which is dependent on T_e. The values of k can be found in the literature either directly or by integrating known cross sections over the electron energy distribution (assumed here to be Maxwellian, with T_e measured by the Langmuir probe). The reactions considered, along with the sources used for the rate constants, are as follows (Table 1).

These reactions produced gains and losses inside the domain, to be plugged into rate equations of the form of Eq. (3). While this is not an exhaustive set of all possible reactions in a hydrogen plasma, this set was chosen as the most relevant because of comparatively high reaction rate constants within the experimental parameter space. It should be noted that reactions R4, R5, and R8 use different reaction rates for production of H radicals at different excitation levels. Excitation states were not tracked in this model; therefore, it was implicitly assumed that excited products undergo relaxation before undergoing more collisions. However, it was necessary to consider the rates in reactions R4, R5, and R8 to accurately model the total H atom creation rate.

3.3 *Surface Gains and Losses*

At this point, only the surface loss and gain terms were left to consider. Due to the assumptions discussed earlier, the only surface loss considered is loss of particles to the collector and through the face opposite of the collector, beyond which the electron density is assumed to be 0. At the collector, radicals

Table 1 Volumetric reactions considered in the 0-D model are shown, along with references from which the rate constants k were either calculated directly or derived.

Reaction number	Reaction	Source
(R1)	$H_2^+ + H_2 \xrightarrow{k_1} H_3^+ + H$	23
(R2)	$H_2^+ + e \xrightarrow{k_2} 2H$	24
(R3)	$H_3^+ + e \xrightarrow{k_3} H_2 + H$	24
(R4)	$H_2 + e \xrightarrow{k_4} 2H + e$	25
(R5)	$H_2 + e \xrightarrow{k_5} 2H + e$	25
(R6)	$H + e \xrightarrow{k_6} H^+ + 2e$	26
(R7)	$H_3^+ + e \xrightarrow{k_7} 2H + H^+ + e$	26
(R8)	$H_2 + e \xrightarrow{k_8} 2H + e$	25,27,28

will be lost to the wall via recombination, which will occur with a probability γ

$$2H + \text{Wall} \rightarrow H_2. \tag{4}$$

The value of γ was chosen to be 0.07, in agreement with the general range for γ that is cited in the literature.[20] Additionally, the radicals reach the surface through isodirectional thermal motion. Thus, the flux of radicals lost to the collector will be as shown in

$$\Gamma_{\text{radical loss to collector}} = \gamma \frac{1}{4} n_H v_H. \tag{5}$$

Ions do not reach the collector by random motion. Rather, they are accelerated toward the collector by the plasma sheath and presheath, causing a directed ion flux. Ions are assumed to be lost with a probability of 1. Thus, the ion loss flux to the collector is given by

$$\Gamma_{\text{ion loss to collector}} = n_i v_B. \tag{6}$$

In this equation, v_B is the Bohm velocity, given by

$$v_B = \sqrt{\frac{T_i q_i}{m_i}}, \tag{7}$$

where T_i is the ion temperature (assumed to be room temperature), q_i is the ion charge, and m_i is the ion mass.

While ions are lost when they hit the collector, the mechanism of loss can vary. Ions can implant, stick to the surface, or be reflected. Reflection of H_2^+ simply produces neutral H_2. However, reflections of H^+ and H_3^+ occur according to[22]

$$H^+ + \text{Wall} \rightarrow H, \tag{8}$$

$$H_3^+ + \text{Wall} \rightarrow H + H_2. \tag{9}$$

Equations (8) and (9) represent radical gain mechanisms. Reflection probabilities were determined by the Monte

Downloaded From: https://www.spiedigitallibrary.org/journals/Journal-of-Micro/Nanolithography,-MEMS,-and-MOEMS on 6/13/2018 Terms of Use: https://www.spiedigitallibrary.org/terms-of-use

Table 2 Reflection of incident H^+ [Eq. (8)] and H_3^+ [Eq. (9)] produces H radicals. Reflection coefficients, determined by SRIM, are shown at different pressures.

Pressure (mTorr)	Eq. (8)	Eq. (9)
65	0.30	0.34
97.5	0.30	0.35
130	0.31	0.35

Carlo code known as the stopping and range of ions in matter (SRIM).[29] Ion energies were assumed to be the difference between the plasma potential and the average collector voltage, as measured by a high-voltage probe. At 65-mTorr, the energy was 350 eV. At 325 mTorr, the energy was 150 eV. For pressures between those two values, the energy was assumed to vary linearly with pressure. For the dissociative reflection of H_3^+, the reflection coefficient was determined to be the coefficient of an incident H^+ ion with 1/3 of the energy. Reflection coefficients for Eqs. (8) and (9) are shown in Table 2 for the different pressures used in the 0-D model.

Reflection causes positive radical fluxes into the domain according to

$$\Gamma_{\text{radical gain due to Eq.(8)}} = R_{H^+}\frac{A}{V}n_{H^+}v_{H^+,\text{Bohm}}, \tag{10}$$

$$\Gamma_{\text{radical gain due to Eq.(9)}} = R_{H_3^+}\frac{A}{V}n_{H_3^+}v_{H_3^+,\text{Bohm}}. \tag{11}$$

Fluxes across the surface opposite the collector must also be considered. According to the approximation that there is no plasma beyond that surface, no ions can diffuse from the far side of the surface into the domain. Thus, the surface simply sees an ion loss flux. Since the surface is not a physical wall, there is no sheath, and the ions simply travel isodirectionally at the thermal velocity, as shown in

$$\Gamma_{\text{ion loss across axial boundary}} = \frac{1}{4}n_i v_{\text{th}_i}. \tag{12}$$

Radicals present a somewhat different picture. Once radicals leave the domain through the axial surface, there is only one volumetric method of radical destruction (R6), but since the model assumes an electron density of 0 beyond the surface, R6 cannot proceed. This means that radicals can be lost only to recombination on the walls. The walls are far away from the domain, and the recombination coefficient is very small, causing most radicals to be reflected. For the purposes of this model, it is, therefore, assumed that the radical density is approximately flat near the domain; thus, approximately no radicals are lost across the axial surface.

3.4 *Final System of Equations*

Rate equations of the form of Eq. (3) were then solved for the densities of radicals, H^+ and H_3^+. The density of H_2^+ was calculated by assuming quasineutrality, which states that the sum of the ion densities is equal to the electron density, which was set as an experimentally determined constant based on Langmuir probe measurements. Since the predominant species, by far, is neutral H_2, the density of neutral H_2 was assumed to be a constant dictated by the gas pressure. The final system of equations is shown in

$$\begin{aligned}\frac{dn_H}{dt} &= k_1 n_{H_2} n_{H_2^+} + 2k_2 n_e n_{H_2^+} + k_3 n_e n_{H_3^+} + 2(k_4+k_5)n_{H_2}n_e \\ &\quad + 2k_7 n_e n_{H_3^+} + 2k_8 n_{H_2} n_e - k_6 n_H n_e - \gamma\frac{1}{L}\frac{n_H v_{H,\text{th}}}{4} \\ &\quad + R_{H^+}\frac{1}{L}n_{H^+}v_{H^+,\text{Bohm}} + R_{H_3^+}\frac{1}{L}n_{H_3^+}v_{H_3^+,\text{Bohm}},\end{aligned} \tag{13}$$

$$\frac{dn_{H^+}}{dt} = k_6 n_H n_e + k_7 n_e n_{H_3^+} - \frac{1}{L}n_{H^+}v_{H^+,\text{Bohm}} - \frac{1}{L}\frac{n_{H^+}v_{H^+,\text{th}}}{4}, \tag{14}$$

$$\frac{dn_{H_2^+}}{dt} = n_e - n_{H^+} - n_{H_3^+}, \tag{15}$$

$$\begin{aligned}\frac{dn_{H_3^+}}{dt} &= k_1 n_{H_2} n_{H_2^+} - k_3 n_e n_{H_3^+} - k_7 n_e n_{H_3^+} \\ &\quad - \frac{1}{L}n_{H_3^+}v_{H_3^+,\text{Bohm}} - \frac{1}{L}\frac{n_{H_3^+}v_{H_3^+,\text{th}}}{4}.\end{aligned} \tag{16}$$

These equations were solved in MATLAB by running ode15s until convergence at steady state.

3.5 *Model Calibration and Error*

At 65 mTorr and 300 W, simultaneously solving Eqs. (13)–(16) yielded the following values for the four dependent variables: $n_H = 4.21\times10^{12}\ \text{cm}^{-3}$, $n_{H+} = 2.50\times10^5\ \text{cm}^{-3}$, $n_{H2+} = 1.56\times10^8\ \text{cm}^{-3}$, and $n_{H3+} = 7.96\times10^9\ \text{cm}^{-3}$. At this point, it is appropriate to comment on the choice of $\gamma = 0.07$ as the recombination coefficient. Sources in the literature present a wide range of values for γ from 0.01–0.2. To ensure simulation consistency, only one value from this range must be chosen; however, due to this large range, the choice of γ can have a large effect on the simulated radical density. The value of 0.07 falls in the middle of this range; additionally, Refs. 30 and 31 cite 0.07 exactly as the recombination coefficient for H radicals on stainless steel. Finally, $\gamma = 0.07$ yields a very close match between experimental and model radical densities at this condition ($4.3\times10^{12}\ \text{cm}^{-3} \pm 4\times10^{11}\ \text{cm}^{-3}$ versus $4.21\times10^{12}\ \text{cm}^{-3}$, respectively). Thus, the choice of γ was informed by and is in strong agreement with both the literature and experiments.

Once set to 0.07, γ was held constant throughout all simulations. For the purposes of error analysis, γ will be assumed to be a set, fixed constant. Model error presented as error bars on radical density graphs will be due to parameters that are not set but instead are measured variables. Most error is due to small uncertainties (ranging from 0.25 to 0.5 eV) in T_e, since T_e enters Eqs. (13)–(16) through an exponential in the Maxwellian electron energy distribution used to calculate the reaction rate coefficients.

Downloaded From: https://www.spiedigitallibrary.org/journals/Journal-of-Micro/Nanolithography,-MEMS,-and-MOEMS on 6/13/2018 Terms of Use: https://www.spiedigitallibrary.org/terms-of-use

4 Results and Discussion

Radical probe experiments were carried out for variations in power, pressure, and flow. For each experiment, radical densities were measured with the catalytic probe, while electron density and electron temperature were measured with the Langmuir probe; the measured n_e and T_e values were then plugged into the model, which calculated predicted radical densities.

The base conditions were 300-W RF power, 65 mTorr, and 1000 sccm of H_2 flow. While a given parameter was varied, the other parameters were left at their base values, unless otherwise noted. Additionally, Sn removal rates were carried out at 325 mTorr at flow rates of 1000 and 3200 sccm. These will be compared to results published in another paper at 65 mTorr and 500 sccm H_2 flow.[11]

4.1 *Power Variation*

Power was varied among 100, 200, and 300 W. Power variation was carried out at two different pressures: 65 and 97.5 mTorr. Experimental and model results at 65 mTorr are compared in Fig. 6.

As expected, experimental n_H is approximately linear with power. Additionally, extrapolating the trend backward would yield approximately 0 radicals at 0-W power. These two facts suggest that the catalytic probe is working as expected. The proper functioning of the probe, as well as an understanding of the science behind radical creation, is confirmed by the agreement between the model output and experiment data. The agreement at 100 and 300 W is particularly close given the level of approximation inherent in a 0-D model.

To further demonstrate the versatility of the model, power variation experiments were also carried out at 97.5 mTorr and are presented in Fig. 7. As with power variation at 65 mTorr, the model is in good agreement with the experimental data.

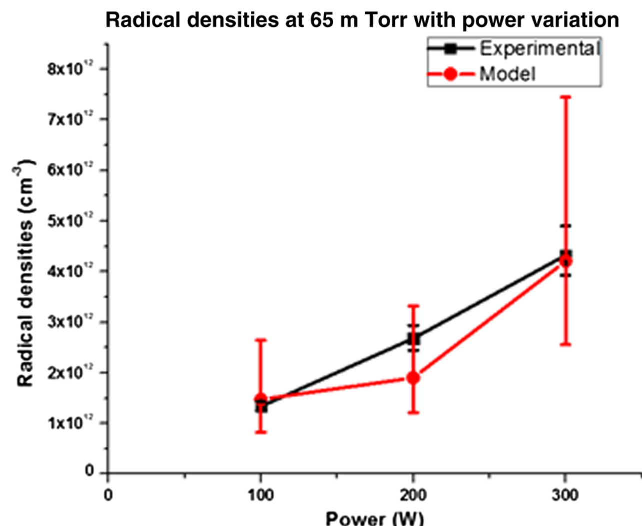

Fig. 6 The predicted and experimental radical densities are shown as a function of power at 65 mTorr. The experimental data are approximately linear with power, as would be expected. The model predictions are in good agreement with the experimental results.

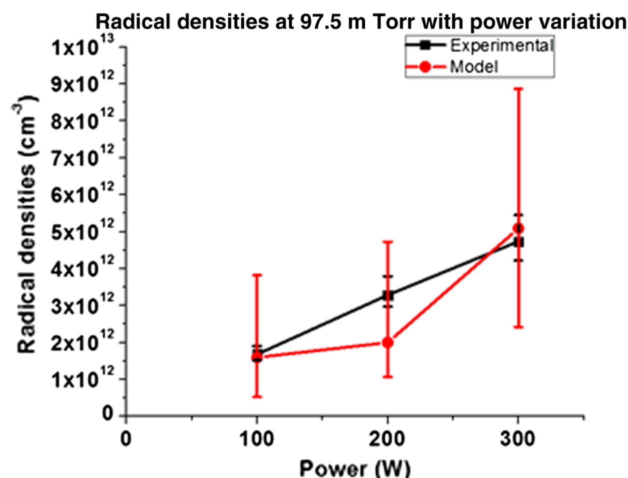

Fig. 7 The predicted and experimental radical densities are shown as a function of power at 97.5 mTorr. As at 65 mTorr, the experimental data are approximately linear with power, as would be expected. Agreement with experiments at a higher pressure suggests that the fundamental science behind radical creation has been captured.

4.2 *Pressure Variation*

With a constant 300 W of RF power, the pressure was varied among 65, 97.5, and 130 mTorr. Model results are contrasted with experimental results in Fig. 8.

Once again, the model agrees well with experiments. Both model and experimental data show that radical density increases with pressure. The agreement between experiment and model shown in Figs. 6–8 confirmed that the probe is working correctly and is a reliable experimental diagnostic.

Increasing the pressure above 130 mTorr reveals that the increase of radical density with pressure is not linear, as shown in Fig. 9. This is due to the fact that the main source of radical creation is the dissociation of H_2 by electrons. While n_{H2} obviously increases with the pressure, n_e experiences a decrease. Thus, the increase of n_H with pressure is not linear. At pressures above 130 mTorr, only experimental results are provided, since increasing the pressure above

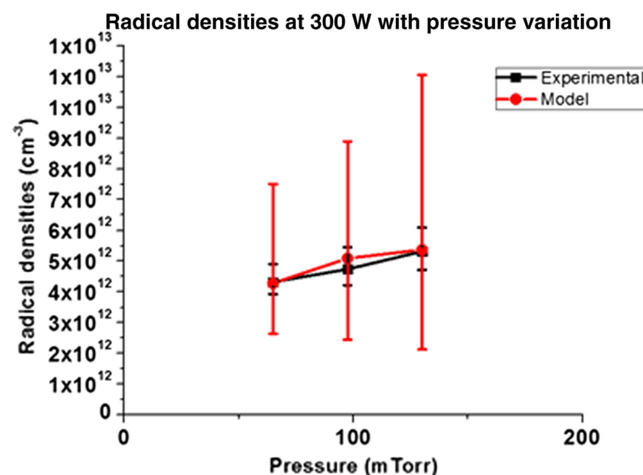

Fig. 8 The predicted and experimental radical densities are shown as a function of pressure at 300 W. When power is varied, the model results agree well with experimental data when pressure is varied.

Downloaded From: https://www.spiedigitallibrary.org/journals/Journal-of-Micro/Nanolithography,-MEMS,-and-MOEMS on 6/13/2018 Terms of Use: https://www.spiedigitallibrary.org/terms-of-use

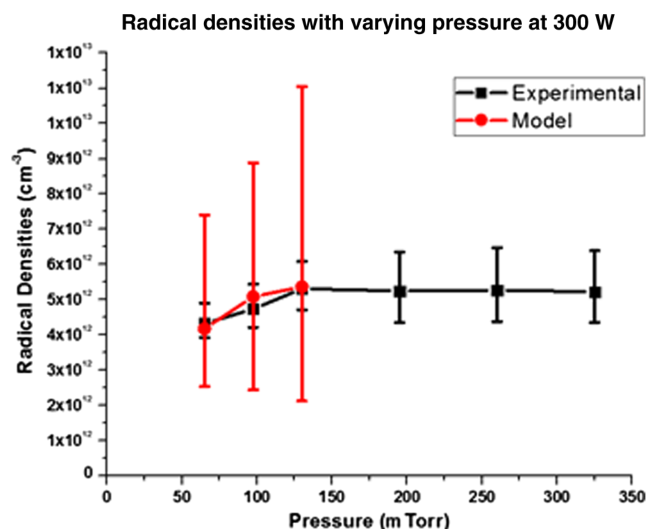

Fig. 9 As pressure increases, radical density generally increases, though not linearly. This is due to decreases in ne at high pressures. At 195, 260, and 325 mTorr, all radical probe results were effectively the same.

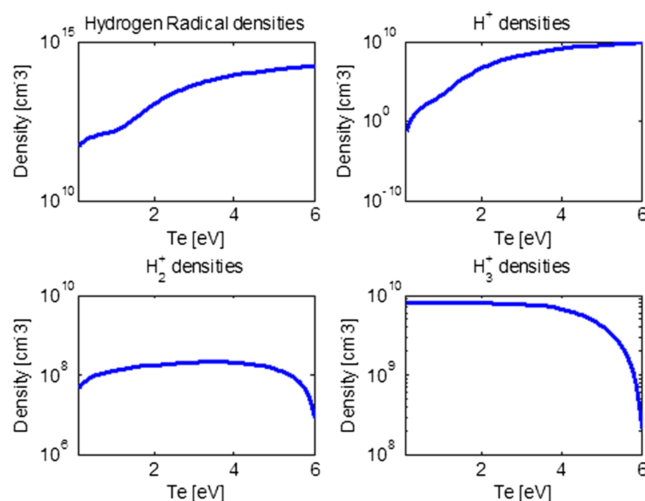

Fig. 10 The model can also predict ion densities. Here, an example is shown at 65 mTorr, 300 W as a function of T_e, which was experimentally measured to be 1.55 eV. At this condition, the measured electron density was 8.12×10^9 cm^{-3}. Thus, this graph indicates that almost all ions are H_3^+. This is consistent with other hydrogen plasma chemistry models in this pressure region.[23]

130 mTorr caused the Langmuir probe sheath to become collisional, leaving the collisionless regime where the model inputs of n_e and T_e can be easily measured with standard collisionless Langmuir probe theory.

4.3 *Flow Variation*

At 325 mTorr and 300 W, radical densities were measured for flow rates of 1000, 1500, 2000, and 3200 sccm (with 3200 sccm being the maximum flow rate possible while maintaining a pressure of 325 mTorr). However, no measurable variation of radical density was visible with flow variation, with the density always being equal to the value presented in Fig. 9 at 325 mTorr (5.2×10^{12} cm^{-3} $\pm$ 1×10^{12} cm^{-3}). This confirmed that, within this range of flow rates, increases in flow did not cause removal of any measurable number of radicals. This agreed with an implicit assumption in the 0-D model, since the model did not account for any method of affecting the radical density by means of flow variation. This assumption was validated by the experiments that showed no change in radical density as a function of flow.

4.4 *Ion Densities*

It should also be noted that the model can also predict ion densities. As an example, ion and radical densities are plotted against electron temperature at 65 mTorr in Fig. 10. At this condition (65 mTorr, 300 W), the electron density was 8.12×10^9 cm^{-3}, and the electron temperature was 1.55 eV.

The ion density results in Fig. 10 show that, at physically relevant values of T_e, virtually all ions are H_3^+. This agrees with other research performed on hydrogen plasma chemistry[23] and helps confirm that the model is operating as expected.

4.5 *Sn Removal Rates*

As seen in Sec. 4.4, radical densities rose when the pressure was increased, though they did not rise linearly. A simple etching model based solely on radical densities would, therefore, predict an increase in Sn removal rates at higher pressures.

However, this was not the case. Etching experiments and etch rate measurements performed in Ref. 11 showed an average etch rate of ~1.1 nm/ min at 65 mTorr, 300 W, and 500 sccm. In this paper, the same procedure was used in an attempt to measure removal rates at 325 mTorr, 300 W, and 1000 sccm. Briefly, witness plates (1 cm^2) were placed on the collector, which was coated with a-50 nm Sn film by magnetron sputtering in a separate chamber. The samples were masked such that half of each sample was coated with Sn, while half was not. Deposition thickness was measured with a quartz crystal monitor. The collector was then moved into XCEED for etching. Witness plate masks were rotated for etching, such that an exposed Sn surface was next to an exposed bare Si surface on each witness plate. Etching was carried out for 2 h. Afterward, the Sn thickness remaining was determined using a surface profilometer by measuring the step height between the exposed Sn and the exposed Si on the witness plates. More information on this setup and procedure is provided in Ref. 11.

At 325 mTorr, 300 W, and 1000 sccm, it was difficult to obtain a consistent and reliable measurement of removal rate with the profilometer. The step size was below the size of the error range (20 to 30 nm). The error of the profilometer is 20 to 30 nm; therefore, the range of error was larger than the measurement. This places an upper bound of 0.25 nm/ min on the etch rate. Secondary electron microscopy images of the as-deposited Sn and the plasma-etched Sn in Fig. 11 do show that the plasma has altered the Sn structure somewhat, however, cleaning has not completed.

To further explore this effect, an etching experiment was performed at 325 mTorr using 3200 sccm, the maximum flow rate that could be handled by the pumping system at that pressure. However, the removal rate was still not measurable by the profilometer. This leads, once again, to an upper bound of 0.25 nm/ min.

Downloaded From: https://www.spiedigitallibrary.org/journals/Journal-of-Micro/Nanolithography,-MEMS,-and-MOEMS on 6/13/2018 Terms of Use: https://www.spiedigitallibrary.org/terms-of-use

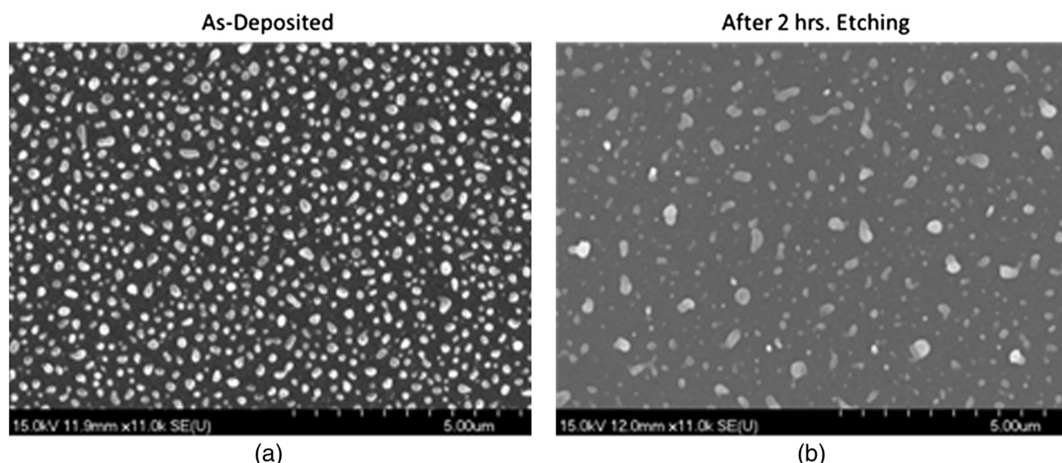

Fig. 11 (a) The witness plate surface is coated with Sn before etching. (b) After 2 h of etching at 325 mTorr and 1000 sccm of H_2 flow, some Sn has been removed, but some is still on the surface. This indicates an incomplete etch.

When compared to the previous 65 mTorr results of 1.1 nm/ min,[11] it is clear that etching at 325 mTorr occurs far slower than at 65 mTorr, even though the radical density does not decrease as the pressure is increased between these two values. Thus, the radical densities measured in this paper show that Sn removal is not a function of radical density alone, and radical density is not the limiting factor within this parameter space. In order to determine what limits Sn removal rate, an investigation into other factors must be performed. One potential factor is redeposition. SnH_4 is known to be unstable and dissociate at room temperature upon collision with a wall.[32,33] As the pressure is increased, the mean free path for SnH_4 molecules will be decreased, subjecting them to more frequent collisions and making it more likely that they will simply be reflected back onto a wall rather than pumped out. Another potential factor is ion bombardment. Energetic ions are known to accelerate etching by breaking surface bonds and allowing etchant species to bond to the surface atoms.[34] Decreases in the ion energy and ion current to the surface at high pressures could cause decreases in the removal rate. Studies of these processes will be presented in a future paper. Additionally, a more sensitive measurement technique will need to be used to more fully characterize the low etch rates at high pressures.

5 Conclusions

An investigation of the science behind radical creation in a capacitively coupled plasma source for *in situ* EUV collector cleaning has been developed. This source constitutes a plasma etching source to remove Sn by reaction with H radicals. A 0-D plasma chemistry model was created to predict H radical densities in the nontraditional plasma chamber geometry of XCEED. This model was shown to agree with catalytic probe experiments, validating the catalytic probe as a reliable experimental technique. Experiments were carried out on radical density variation as a function of power, pressure, and flow. Radical densities were observed to increase linearly with power, increase nonlinearly with pressure, and remain constant with flow rate for the ranges explored in this paper.

It was also observed that Sn removal rates did not track radical densities. An increase in pressure caused the removal rate to drop from 1.1 nm/ min at 65 mTorr to a level below the error bar of the measuring instrument (0.25 nm/ min) at 325 mTorr, despite providing a modest increase in radical density. Based on these results, H radical density is shown not to be the limiting factor in Sn removal. It is thought that the decrease of etch rate at high pressure is caused by an alteration in the etching process (such as a decrease in ion energy and ion current) or the dissociation of SnH_4 upon wall impact (and subsequent redeposition of Sn). Thus, having provided an understanding of radical creation in this paper, future research will focus on understanding SnH_4 removal.

Acknowledgments

This work was supported by the National Science Foundation under Grant No. 14-36081. Additionally, the authors are grateful for funding and support from Cymer, LLC. The authors would also like to thank undergraduate students Valentin Castro, Shanna Bobbins, and Sean Piper for their help in carrying out experiments. Parts of this research were carried out in the Frederick Seitz Materials Research Laboratory Central Facilities, University of Illinois, which is partially supported by the U.S. Department of Energy under Grant Nos. DEFG02-07ER46453 and DE-FG02-07ER46471.

References

1. G. E. Moore, "Progress in digital integrated electronics," in *Int. Electron Devices Meeting*, Vol. **21**, pp. 11–13 (1975).
2. M. Rothschild et al., "Recent trends in optical lithography," *Lincoln Lab. J.* **14**(2), 221–236 (2003).
3. S. Novak et al., "Transistor aging and reliability in 14nm tri-gate technology," in *IEEE Int. Reliability Physics Symp.* (2015).
4. E. R. Hosler et al., "Considerations for a free-electron laser-based extreme-ultraviolet lithography program," *Proc. SPIE* **9422**, 94220D (2015).
5. R. A. Burdt et al., "Laser wavelength effects on the charge state resolved ion energy distributions from laser-produced Sn plasma," *J. Appl. Phys.* **107**(4), 043303 (2010).
6. A. A. Schafgans et al., "Performance optimization of MOPA pre-pulse LPP light source," *Proc. SPIE* **9422**, 94220B (2015).
7. J. Sporre and D. N. Ruzic, "Debris transport analysis at the intermediate focus of an extreme ultraviolet light source," *J. Micro/Nanolithogr., MEMS, MOEMS* **11**(2), 021117 (2012).
8. C. Hecquet et al., "Design, conception, and metrology of EUV mirrors for aggressive environments," *Proc. SPIE* **6586**, 65860X (2007).

Downloaded From: https://www.spiedigitallibrary.org/journals/Journal-of-Micro/Nanolithography,-MEMS,-and-MOEMS on 6/13/2018 Terms of Use: https://www.spiedigitallibrary.org/terms-of-use

9. H. Maury et al., "Non-destructive x-ray study of the interphases in Mo/Si and Mo/B4C/Si/B4C multilayers," *Thin Solid Films* **514**(1–2), 278–286 (2006).
10. D. T. Elg et al., "Magnetic debris mitigation system for EUV sources," *J. Micro/Nanolith. MEMS MOEMS* **14**(1), 013506 (2015).
11. D. T. Elg et al., "In-situ collector cleaning and EUV reflectivity restoration by hydrogen plasma for EUV sources," *J. Vac. Sci. Technol. A* **34**, 021305 (2016).
12. K. C. Thompson et al., "Experimental test chamber design for optics exposure and debris characterization of a xenon discharge produced plasma source for extreme ultraviolet lithography," *Microelectron. Eng.* **83**, 476–484 (2006).
13. E. L. Antonsen et al., "Ion debris characterization from a z-pinch extreme ultraviolet source," *J. Appl. Phys.* **99**, 063301 (2006).
14. D. N. Ruzic, *Electric Probes for Low-Temperature Plasmas*, AVS Press, New York (1994).
15. A. Drenik et al., "Recombination of hydrogen atoms on fine-grain graphite," *Appl. Surf. Sci.* **257**, 5820–5825 (2011).
16. M. Mozetic et al., "Determination of density of hydrogen atoms in the ground state," *Vacuum* **47**(6–8), 943–945 (1996).
17. M. Mozetic et al., "An iron catalytic probe for determination of the O-atom density in an Ar/O2 afterglow," *Plasma Chem. Plasma Process.* **26**, 103–117 (2006).
18. M. Mozetic et al., "Catalytic probes for measuring H distribution in remote parts of hydrogen plasma reactors," *J. Nucl. Mater.* **363–365**, 1457–1460 (2007).
19. A. Bogaerts et al., "Computer modelling of the plasma chemistry and plasma-based growth mechanisms for nanostructured materials," *J. Phys. D: Appl. Phys.* **44**(17), 174030 (2011).
20. S. Kim et al., "Improved volume-averaged model for steady and pulsed-power electronegative discharges," *J. Vac. Sci. Technol., A* **24**(6), 2025–2040 (2006).
21. E. Despiau-Pujo et al., "Pulsed Cl_2/Ar inductively coupled plasma processing: 0D model versus experiments," *J. Phys. D: Appl. Phys.* **47**(45), 455201 (2014).
22. M. Sode et al., "Ion chemistry in H_2-Ar low temperature plasmas," *J. Appl. Phys.* **114**, 063302 (2013).
23. I. Mendez et al., "Atom and ion chemistry in low pressure hydrogen DC plasmas," *J. Phys. Chem. A* **110**(18), 6060–6066 (2006).
24. J. Perrin et al., "Cross-sections, rate constants, and transport coefficients in silane plasma chemistry," *Contrib. Plasma Phys.* **36**(1), 3–49 (1996).
25. S. Buckman and A. Phelps, "Vibrational exciation of D_2 by low energy electrons," *J. Chem. Phys.* **82**(11), 4999–5011 (1985).
26. R.K. Janev et al., *Elementary Processes in Hydrogen-Helium Plasmas*, Springer-Verlag, New York (1987).
27. S. Biagi, "v8.9 FORTRAN MAGBOLTZ database," 2010, www.lxcat.net/Biagi (15 February 2016).
28. Y. Itikawa, "Itikawa database," 2012,www.lxcat.net/itikawa (15 February 2016).
29. J.F. Ziegler et al., *SRIM–The Stopping and Range of Ions in Matter*, Lulu Press Company, Morrisville, North Carolina (2008).
30. M. Mozetic et al., "Recombination of neutral hydrogen atoms on AISI 304 stainless steel surface," *Appl. Surf. Sci.* **144–145**, 399–403 (1999).
31. J. Jolly and J.P. Booth, "Atomic hydrogen densities in capacitively coupled very high-frequency plasmas in H_2: Effect of excitation frequency," *J. Appl. Phys.* **97**, 103305 (2005).
32. E. G. Rochow and E. W. Abel, "The chemistry of germanium, tin and lead," in *Pergamon Texts in Inorganic Chemistry*, p. 59, Oxford, England (1973).
33. K. Tamaru, "The thermal decomposition of tin hydride," *J. Phys. Chem.* **60**(5), 610–612 (1956).
34. J. W. Coburn and H. F. Winters, "Plasma etching—a discussion of mechanisms," *J. Vac. Sci. Technol.* **16**(2), 391–403 (1979).

Daniel T. Elg earned his PhD as a Mavis Future Faculty Fellow in the Department of Nuclear, Plasma, and Radiological Engineering at the University of Illinois at Urbana-Champaign. His graduate research focused on debris management strategies for EUV systems. Currently, he is performing postdoctoral research studying atmospheric-pressure plasma, plasma control, and plasma-liquid interactions for medical applications at the University of California, Berkeley. His research interests include low-temperature plasma science, plasma processing applications, and plasma–material interactions.

Gianluca A. Panici is a student at the University of Illinois pursuing his PhD in nuclear, plasma, and radiological engineering. He is also an IBM PhD fellow. He is interested in plasma processing for semiconductor manufacturing and potential plasma solutions to increase EUV source availability.

Jason A. Peck is a PhD candidate in the Nuclear, Plasma, and Radiological Engineering Department at the University of Illinois. His work has focused on novel plasma processing techniques—specifically surface wave PECVD for photovoltaics, laser-assisted plasma etch, and computational work in plasma chemistry and source design. Inspired by industry-driven innovation, he will be joining Intel's Components Research Team upon graduation mid-2017.

Shailendra N. Srivastava received his PhD from the Technische Universitaet Kaiserslautern, Germany, in experimental physics, where he worked extensively on laser-produced plasmas. He worked as a postdoctoral fellow in the Department of Nuclear, Plasma, and Radiological Engineering at the University of Illinois at Urbana-Champaign. He has been working in the semiconductor industry for many years on EUV source development EUV collector contamination and mitigation. His research interests are plasma–material interactions, laser–material interactions, and metrology development.

David N. Ruzic is the Abel Bliss professor of Nuclear, Plasma, and Radiological Engineering, and the director of the Center for Plasma Material Interactions at the University of Illinois at Urbana-Champaign. He is a fellow of the American Nuclear Society, the American Vacuum Society (AVS), and the Hertz Foundation. He also serves as the scientific director for the International Union of Vacuum Science, Techniques, and Applications.

Downloaded From: https://www.spiedigitallibrary.org/journals/Journal-of-Micro/Nanolithography,-MEMS,-and-MOEMS on 6/13/2018 Terms of Use: https://www.spiedigitallibrary.org/terms-of-use